Research paper

Effects of grid alignment on modeling the spray and mixing process in direct injection diesel engines under non-reacting operating conditions

Amin Maghbouli*, Tommaso Lucchini, Gianluca D'Errico, Angelo Onorati

Internal Combustion Engine Group, Dipartimento di Energia, Politecnico di Milano, Via Lambruschini 4, 20156 Milan, Italy

Received 14 May 2015
Accepted 13 July 2015
Available online 29 July 2015

Nomenclature

D	diffusion coefficient
k	turbulent kinetic energy
t	time
u	velocity vector
Z	mixture fraction
Z''	mixture fraction variance

Subscripts

i	X, Y, and Z dimensions

Greek symbols

C_χ	model constant
ε	turbulent kinetic energy dissipation rate
ρ	density
$\dot{\rho}^S$	source term due to spray
ϕ	equivalence ratio
μ	turbulent viscosity
$\tilde{\chi}$	mean scalar dissipation rate

Abbreviations

ATDC	after top dead center
CAD	crank angle degree
CFD	computational fluid dynamics
DI	direct injection
DOI	duration of injection
EGR	exhaust gas recirculation
EVO	exhaust valve opening
HCCI	homogeneous charge compression ignition
ICE	internal combustion engine
IVC	inlet valve closure
LDEF	Lagrangian-droplet and Eulerian-flow field
NO_x	nitrogen oxides
PCCI	premixed charge compression ignition
PM	particulate matter
PPCI	partially premixed compression ignition
Sc	turbulent Schmidt number
SOI	start of injection
UHC	unburnt hydrocarbons

* Corresponding author.
E-*mail address:* amin.maghbouli@polimi.it (A. Maghbouli).

1. Introduction

Flame structure and pollutant formation in conventional and advanced combustion modes in diesel engines were mainly determined by the characteristics of spray evolution and air−fuel mixing processes. The high number of interacting physical and chemical phenomena which take place during the fuel injection and combustion has motivated over the years a significant interest towards the use of CFD tool for both diagnostic and design purposes [1−5]. Many efforts were carried out in order to improve available turbulence and spray models in CFD codes. However, enhance-ments in physical modeling can be drastically affected by how the CFD grid was structured. Grid quality can negatively influence the prediction of the organized charge motion structures, turbulence generation and interaction between in-cylinder flows and injected sprays. This was even more relevant for applied modern strategies in DI engines, where multiple injections and control of charge motions were employed. The first requirement for accurate DI en-gine simulations is the capacity to well describe the fuel spray processes. Liquid fuel sprays have been widely simulated by the use of Lagrangian-Droplet and Eulerian-Flow field (LDEF) with proper coupling of these two approaches [6−9]. Thus far, Euler-ian−Eulerian approach with an adapted grid was not practical and LDEF was the most applicable approach in terms of computational costs and numerical accuracy [10,11], but it has high sensitivity to the applied numerical grid. In Eulerian-Flow field point of view, further refinements in the size of computational grid are desirable due to more accurate calculations of discretized differential equa-tions and better resolved spatial gradients of the flow quantities. However, here accurate spray simulations would not necessarily be resulted by applying finer grids due to inadequate space resolution of the velocity, temperature and vapor concentration of the fluid flow in the Eulerian phase. This hinders accurate Eulerian flow calculations in the vicinity of the injector nozzle where very high velocity and density gradients were presented. Numerical diffusion introduced by applying coarse and misaligned grids would be the main reason on inaccurate liquid and vapor penetrations and poor modeling of air−fuel mixing no matter how accurate turbulence and spray sub-models were considered. By the experiments it has been known that high pressure diesel spray has a conical morphology during its evolution, although it can be partially or fully deviated by engine swirl and counter squish flows of the piston bowl [12,13]. Alignment of computational mesh on the spray pattern can then ensure realistic spray mixing and morphology. Li et al. [14] investigated the effect of three different combustion chamber geometries on combustion and emission characteristics of a DI diesel engine. Spray oriented computational grid resulted in better accuracy of spray and combustion simulations. Similar studies using spray oriented grids were reported in several re-searches [3,15−17]. Imamori et al. [18] compared effect of polar and non-polar sector meshes on combustion characteristics of SANDIA optically accessible diesel engine. Polar mesh and non-polar meshes were refined and higher mesh resolutions showed better agreement in terms of combustion and emission characteristics with the experimental data. Adaptive Mesh Refinement (AMR) scheme was used by number of researchers [6,19−21] with the objective to reduce the numerical diffusivity by increasing the resolution of the mesh. Lippert et al. [22] performed a compre-hensive study on momentum coupling of liquid and gas phases enabling accurate spray liquid penetrations for coarse meshes. They used adaptive mesh refinement on spray tip penetration simula-tions but no data was provided regarding to the air−fuel mixing and final evaporated spray structure through the application of AMR. Most of the mentioned studies were closely examined spray sub-models, phase coupling and effect of mesh refinement on the spray and combustion predictions. However, less attention was given to the level of accuracy on the moment of final delivery of Lagrangian phase to the Eulerian phase in case of evaporated spray structure and air−fuel mixing. This could be a critical issue while modeling early injection engine operating modes such as PCCI combustion. In such modes, using coarse cells on axial direction and non-spray oriented grids can produce highly reticulated vaporized spray structure and very poor modeling of the air−fuel mixing process. This was noticeably far from actual evaporated spray morphology and can highly reduce the accuracy of mixing and subsequent combustion and emission formation simulations. Multi-dimensional modeling of PCCI mode was investigated by a number of studies [23−27]; however, despite applying very early injections such as −90 CAD ATDC, no attention was given to the grid alignment and its essential effect in air−fuel mixing. Aim of the present work is to introduce a novel approach base on the use of a conical mesh structure in order to get reliable predictions on air-−fuel mixing, equivalence ratio, and scalar dissipation rate distri-butions within the combustion chamber of DI diesel engines. The present work focuses on the non-reacting spray simulations and validations on mixture fraction and liquid/vapor fuel penetrations

as essential mixing parameters which their accuracy represents a fundamental pre-requisite to model the combustion process.

2. Numerical simulation

Multi-dimensional CFD simulations were conducted using the OpenFOAM® [28] open-source code in conjunction with Lib-ICE which is a set of libraries and solvers for comprehensive ICE simulations developed by Internal Combustion Engine Group of Politecnico di Milano [29,30]. LDEF was used in the spray simulations with proper 'gas-to-liquid' and 'liquid-to-gas' coupling sequences. Interpolation process at the parcel locations where the gas quantities were estimated was taken into account in the former sequence. The latter sequence refers to the summation of the particle source terms in the Eulerian conservation laws. For the detailed descriptions of Eulerian and Lagrangian governing equations, their coupling, discretizations, and solution approaches the reader was referred to Refs. [6,31]. Although reacting flow and combustion modeling were not considered in this study, solution of transport equations for Z as mixture fraction and Z'' as its variance was also performed along with mass, momentum and energy conservation equations together with turbulence to evaluate how grid structure might affect the combustion process. Transport equation of Z without turbulence consideration is in form of Eq. (1).

$$\frac{\partial \rho Z}{\partial t} + \frac{\partial}{\partial x_i}(\rho u_i Z) = \frac{\partial}{\partial x_i}\left(\rho D \frac{\partial Z}{\partial x_i}\right) \tag{1}$$

By considering turbulent flow and Favre averaging transport equations of Z and Z'' can be written as it was represented in Eqs. (2) and (3), respectively.

$$\frac{\partial\left(\overline{\rho}\tilde{Z}\right)}{\partial t} + \frac{\partial\left(\overline{\rho}\tilde{u}_i\tilde{Z}\right)}{\partial x_i} = \frac{\partial}{\partial x_i}\left(\frac{\mu}{Sc_{\tilde{Z}}}\frac{\partial \tilde{Z}}{\partial x_i}\right) + \dot{\rho}^s \tag{2}$$

$$\frac{\partial\left(\overline{\rho}\widetilde{Z''^2}\right)}{\partial t} + \frac{\partial\left(\overline{\rho}\tilde{u}_i\widetilde{Z''^2}\right)}{\partial x_i} = \frac{\partial}{\partial x_i}\left(\frac{\mu}{Sc_{\widetilde{Z''^2}}}\frac{\partial \widetilde{Z''^2}}{\partial x_i}\right) + \frac{2\mu}{Sc_{\widetilde{Z''^2}}}(\nabla \overline{Z})^2 - \overline{\rho}\tilde{\chi} \tag{3}$$

In Eq. (3), $\tilde{\chi}$, is the mean scalar dissipation rate which introduces the turbulence–chemistry interactions in modeling of non-premixed turbulent combustion.

$$\tilde{\chi} = C_\chi \frac{\tilde{\varepsilon}}{\tilde{k}} \widetilde{Z''^2} \tag{4}$$

As stated by different authors [32–34] and extensively validated with experimental data, flame structure in diesel engines can be represented by an ensemble of diffusion flames, where the scalar dissipation rate parameter was found to govern sub-grid mixing between air and fuel with a consequent effect on flame extinction, auto-ignition time and heat release rate during mixing controlled combustion phase [35]. Hence effect of mesh structure, resolution and alignment on scalar dissipation rate distribution is worth to be investigated.

2.1. Simulation case properties and setup

In order to show maximum level of agreement between numerical non-reacting simulations and available experimental data, published experiments of Singh et al. [7] were used in this study. Four stroke Cummins DI diesel engine were used where the optical access to the combustion chamber was provided by an extended piston and flat piston-crown window and imaging access was provided through one of two exhaust valves in the cylinder head. Type 2 Diesel fuel has been used in the experiments whose properties are provided in Table 1. Different modes of combustion were investigated by making changes in the extent of dilution and the relative difference between duration of injection and ignition delay [7,36]. Two laser beams overlapped and directed in a form of less than 1 mm thick laser sheet into the combustion chamber in a way to capture images from the chamber at slope of 14° from the fire deck. This angle was the spray injection angle with respect to fire deck, so the attempt was to capture the laser sheet images on the axis of the spray [37]. In the present study, mesh generation and multi-dimensional simulations were performed on the engine specifications and experimental case properties are listed in Tables 2 and 3, respectively. Non-reacting flow and spray simula-tions were performed using OpenFOAM® and Lib-ICE libraries where summary of applied sub-models is provided in Table 4. It should be noted that engine experiments were conducted under reacting conditions and the represented numerical simulations in this study can be compared with the corresponding experimental cases during the initial air–fuel mixing from start of injection to start of ignition. Complementary explanations regarding mathe-matical description of spray sub-models and their selection were provided in Ref. [6].

2.2. Mesh types

Specifications of four types of computational grids are presented in Table 5. After the grid generation all the meshes were checked on a closed cycle simulations, from IVC to EVO, to have the same

Table 1
Properties of ultra-low sulfur 2007 emissions certification type 2 diesel fuel [7].

Total aromatics by volume	27%
Olefins	0.5%
Saturates	72.5%
Sulfur (by weight)	9.1 ppm
Distillation temperatures	
Initial boiling point	190 °C
10% Distillation temperature	212 °C
50% Distillation temperature	254 °C
90% Distillation temperature	315 °C
End point	350 °C
Cetane number	46
Specific gravity @ 20 °C	0.8426
C/H by weight	6.5
Net heat of combustion	43 MJ/kg
Viscosity @ 40 °C	2.35 cS

Table 2
SANDIA optical engine specifications taken from Ref. [7].

Engine base type	Cummins N-14. DI diesel
Number of cylinders	1
Combustion chamber	Quiescent, DI
Swirl ratio	0.5
Bore × Stroke	13.97 × 15.24 [cm]
Bowl width × depth	9.78 × 1.55 [cm]
Displacement	2.34 [l]
Connecting rod length	30.48 [cm]
Geometric compression ratio	11.2:1
Fuel injector, no. of holes	Common-rail, 8
Spray pattern included angle	152°
Injection pressure	1200/1600 [bar]
Nozzle orifice diameter	0.196 [mm]
Nozzle orifice, L/D	5

Table 3
Properties of the experimental cases taken from Ref. [7].

	Low-temperature late injection	High-temperature long ignition delay	Low-temperature early injection
Engine speed [rpm]	1200	1200	1200
Indicated mean effective pressure [bar]	4.1	4.5	3.9
Injection pressure [bar]	1600	1200	1600
Intake temperature [K]	343	320	363
BDC temperature [K]	351	335	365
Intake pressure [bar]	2.02	1.92	2.14
TDC motored temperature [K]	840	800	870
TDC motored density [kg/m^3]	22.5	22.3	22.9
SOI [°ATDC]	0	−5	−22
DOI [CAD]	7	10	7
Injection quantity [mg/cycle]	56	61	56
O_2 concentration [vol.%]	12.7	21	12.7

Table 4
Summary of applied sub-models/calculation schemes and their properties on multi-dimensional non-reacting diesel engine simulations of this study.

Modeling/calculation of	Applied sub-model/scheme	Sub-model/scheme properties
Turbulence	Standard $k-\varepsilon$ model	Coefficients: $C_\mu = 0.09$, $C_1 = 1.44$, $C_2 = 1.92$, $C_3 = -0.33$
Injection	Huh-injector model [38]	Initial droplet diameter = nominal orifice diameter, $C_d = 0.8$
Spray atomization	Huh–Gosman model [38]	Coefficients: $C_1 = 2.0$, $C_2 = 0.5$, $C_3 = 1.0$, $C_4 = 3.0$, $C_5 = 0.6$, Weber limit = 40
Spray breakup	Kelvin–Helmholtz model [39]	$B_0 = 0.61$, $B_1 = 10$, Weber limit = 6
Spray evaporation	Spalding [6]	D^2-law with relaxation times calculated under standard and boiling conditions
Heat-transfer	Ranz–Marshall [6]	Semi-implicit method for solving droplet energy equation

Table 5
Specifications of the applied computational grid in the non-reacting spray simulations.

Mesh type	Coarse mesh	Fine mesh	Spray oriented mesh	Conical mesh
Number of cells on azimuthal, radial, and axial directions at TDC	21 × 67 × 11	31 × 77 × 23	21 × 77 × 27	17 × variable × variable
Total number of cells at TDC	15,477	54,901	43,659	78,482
Minimum cell volume at TDC [mm^3]	0.0206	0.00494	0.00287	0.00011
Maximum cell volume at TDC [mm^3]	6.12	3.67	5.89	6.95
Minimum cell face area at TDC [mm^2]	0.00696	0.00209	0.000505	0.000581
Maximum cell face area at TDC [mm^2]	5.22	3.66	7.99	6.95

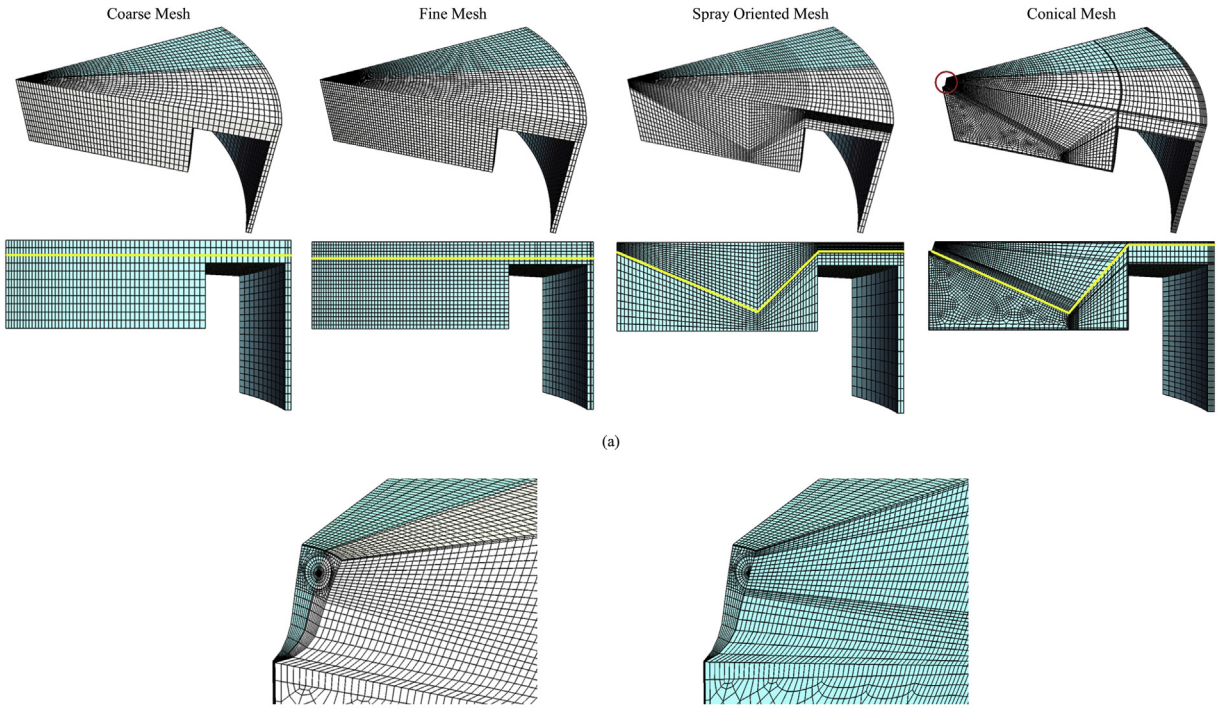

Fig. 1. a) Coarse mesh, fine mesh, spray oriented mesh, and conical mesh generated for SANDIA optical engine geometry, cyan color is the normal view on $y = 0$ cross section. b) Closer view to the cell alignment of conical mesh near the nozzle orifice location, cyan color shows radial alignment of cells on the spray axis (14° below the fire deck). (For interpretation of the references to color in this figure legend, the reader is referred to the web version of this article.)

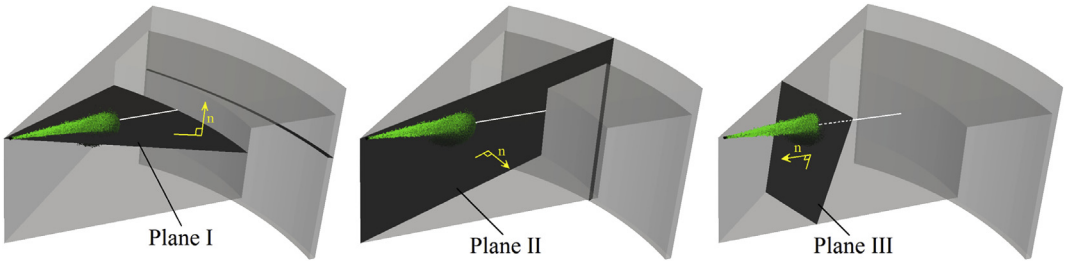

Fig. 2. Geometrical surfaces to extract numerical data. Spray injection direction is shown with spray particles and white lines as the injection axis. Normal vector of Plane I is orthogonal to the injection axis and makes angle of 76° with the cylinder fire deck. Normal vector of Plane II is orthogonal to the injection axis and parallel with the cylinder fire deck. Normal vector of Plane III is parallel to the injection axis with a defined distance from the nozzle orifice.

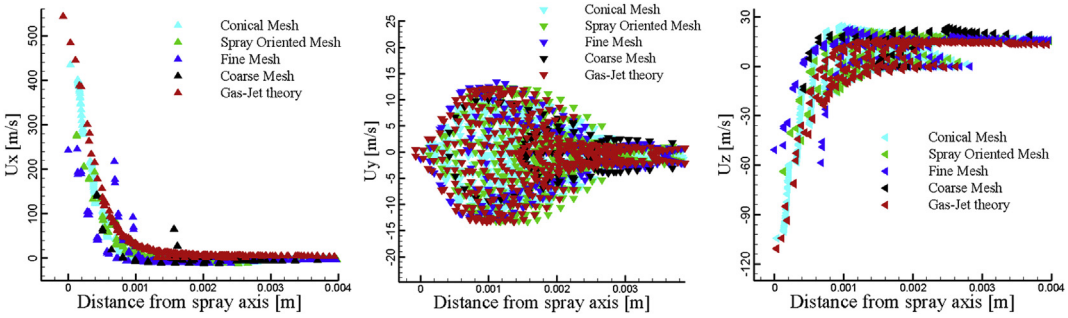

Fig. 3. Grid density function of Eulerian phase velocities of U_x, U_y, and U_z on plane III (located at 4 mm distance from the nozzle orifice) with respect to distance from the cross point of injection axis and Plane III compared to the results of Gas-Jet theory. Distances less than 4 mm from the cross point were considered.

compression ratio of the SANDIA optical engine. Assuming symmetrical combustion chamber geometry, polar Cartesian 45° sector Coarse Mesh was generated for SANDIA optical diesel engine and periodic boundary conditions were assumed on side faces. Fine Mesh was simply generated by refining the Coarse Mesh in radial, azimuthal, and axial directions. These grids are shown in Fig. 1a. It was discussed that spray morphology can be enhanced by aligning the grids on the spray axis. This approach was used to generate a polar Spray Oriented Mesh whose total cell count was less than Fine Mesh. Spray Oriented Mesh is represented in Fig. 1a. In order to get much closer to the conical spray structure, the Conical Mesh shown in Fig. 1a is generated. Presence and geometry of injector in the combustion chamber were also taken into account. A closer view of mesh alignment near the nozzle orifice area is provided in Fig. 1b for the Conical Mesh, where actual nozzle orifice is located in dis-tance of 2 mm from edge of computation grid. In Fig. 1a cyan colored parts are the result of splitting the grids on $y = 0$ plane to show a normal view of the mesh alignments in different introduced meshes. It should be noted that during compression and expansion processes cells were removed and added in both Coarse and Fine Mesh on a flat plate over the bowl, whereas in Spray Oriented and Conical Meshes cell layers were removed and added on a V shaped surface. Cell add/removal layer is shown with a yellow line in Fig. 1a which for Spray Oriented and Conical Meshes allows keeping the cells fixed at TDC and compress/expand the cells below them in any other crank angles. This is a noticeable advantage while simulating engine cases with an early injection such as PCCI modes or multiple injections.

3. Results and discussion

Using the introduced grids and keeping the numerical case setup identical, multi-dimensional closed cycle simulations were first conducted on the Low-Temperature Late-Injection

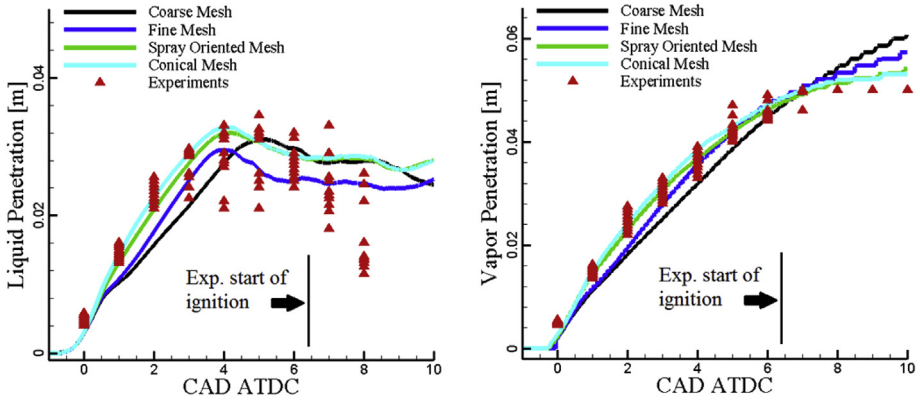

Fig. 4. Liquid and vapor penetration length comparisons between experiments of Singh et al. [7] and numerical simulations of Low-Temperature Late-Injection case using four mesh types in this study.

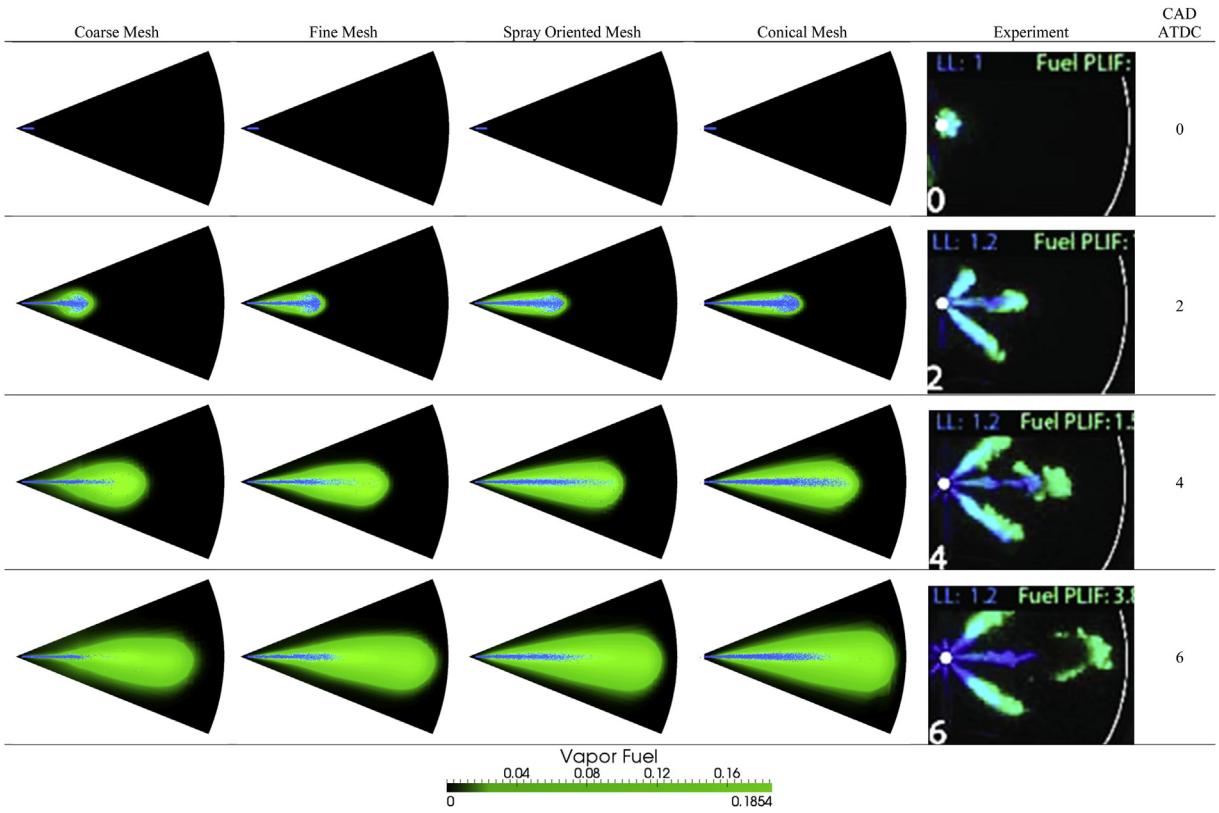

Fig. 5. Simulation results of liquid fuel particles (blue) and vaporized fuel mass fraction (green) distributions on the plane of spray injection axis (normal views of the planes were provided) for four mesh types at 0, 2, 4, and 6 CAD ATDC compared to the experiments of Singh et al. [7]. (For interpretation of the references to color in this figure legend, the reader is referred to the web version of this article.)

experimental case. Results of the simulations were presented in this section.

3.1. Spray behavior near the injector nozzle

It has been discussed that LDEF approach cannot accurately predict momentum exchange between Lagrangian droplets and Eulerian Flow in vicinity of the injector nozzle when the Discrete Droplet Method (DDM) was applied. Instead atomization sub-models were needed to capture the churning flow very close to the nozzle orifice if the dense spray near to the nozzle was not modeled by means of Continuous Droplet Method [40]. In order to include effects of churning flow, Huh–Gosman injector [38] and atomization models were applied. Using the DDM and Huh–Gosman atomization model, effects of dense spray near the nozzle where atomization mainly affected by estimated nozzle turbulence

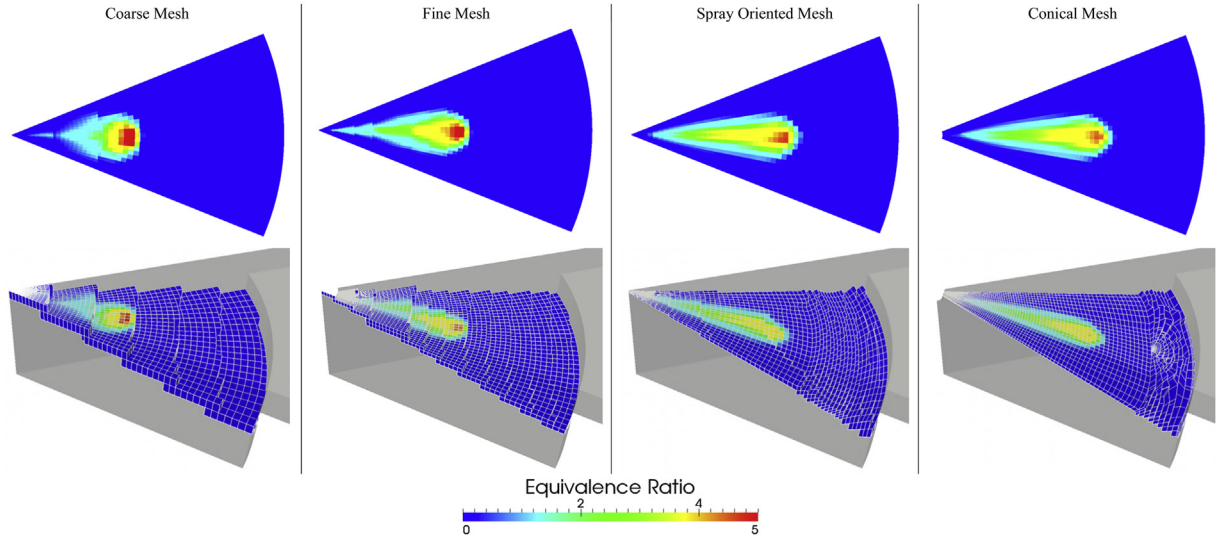

Fig. 6. Top: Equivalence ratio distributions of four mesh types on a normal view of Plane I at 3 CAD ATDC. Bottom: Computational cell alignments within the combustion chamber on the Plane I to capture equivalence ratio distributions in the top row.

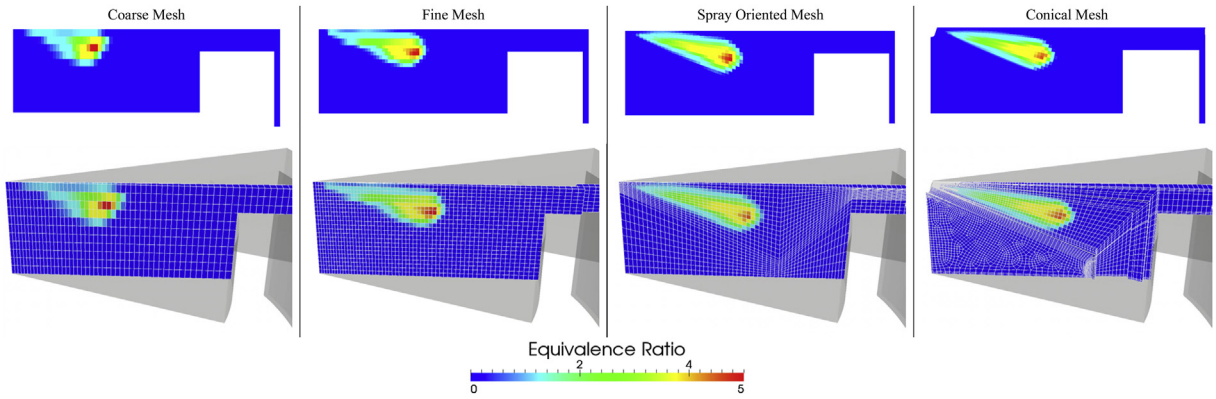

Fig. 7. Top: Equivalence ratio distributions of four mesh types on a normal view of Plane II at 3 CAD ATDC. Bottom: Computational cell alignments within the combustion chamber on the Plane II to capture equivalence ratio distributions in the top row.

both in terms of liquid core length and secondary droplet size can be taken into account. Moreover, 250,000 parcels were considered for the injection event which had increased number of particles per time step. This can better distribute particles within the aligned and conical parts of the grid, keeping the void fraction values under control.

Faeth [40] has shown that by experimental observations liquid core of the spray, L_{fc}, can be estimated by Eq. (5).

$$L_{fc}/d = C_c\left(\rho_f/\rho_\infty\right)^{1/2} \tag{5}$$

where d is injector diameter, C_c is a constant and ρ_f and ρ_∞ are fuel and ambient air densities, respectively. For the applied fuel in this study Eq. (5) yields in liquid core length of 8.2 mm. Depicting the results in this study three critical planes for spray injection are shown in Fig. 2 as Planes I, II and III. These planes will be used to further discuss the results on different aspects. Normal vector of the Plane III is parallel to injection direction vector and in this subsection assumed to be located in a distance of 4 mm from the nozzle orifice. This distance from the nozzle orifice was considered to locate the Plane III within the region where the churning flow is dominant. Fig. 3 shows the grid density function of Eulerian phase velocities in x, y, and z directions with respect to distance from the cross point of injection axis with the Plane III as independent variable for the applied grids. Results of grid types were also compared with Abani et al.'s Gas-Jet model [41] as reference. Density of the number cells for the Conical, Spray Oriented, Fine and Coarse Mesh types on the Plane III with the distance of 4 mm from the nozzle orifice were: 1521, 724, 1022, and 448, respectively. Velocities were shown for the 3 CAD ATDC as the mid of injection duration where the highest liquid fuel mass flow rate takes place. Highest velocities were reported for U_x comparing to velocities in y and z coordinates as the injection axis was just 14° below the fire deck and makes a low angle with the x coordinate. In view of magnitudes of U_x, the Conical Mesh predicts the most similar velocity distributions with Gas-Jet theory comparing to other grid types in vicinity of cross point with the injection axis showing lower numerical diffusion and acceptable momentum exchange between Lagrangian and Eulerian phases. Moreover, it can be seen that there were more distributions for higher U_x velocities for Conical Mesh than other grid types which can suitably take the effect of churning flow into account without directly modeling it through DDM. It is interesting to notice that although grid density on Plane III for Spray Oriented Mesh was almost 30% less than Fine Mesh, the former mesh type managed to capture both higher U_x peak and distribution near the cross point with injection axis. The highest momentum diffusion was reported for the Coarse Mesh where for the distances more

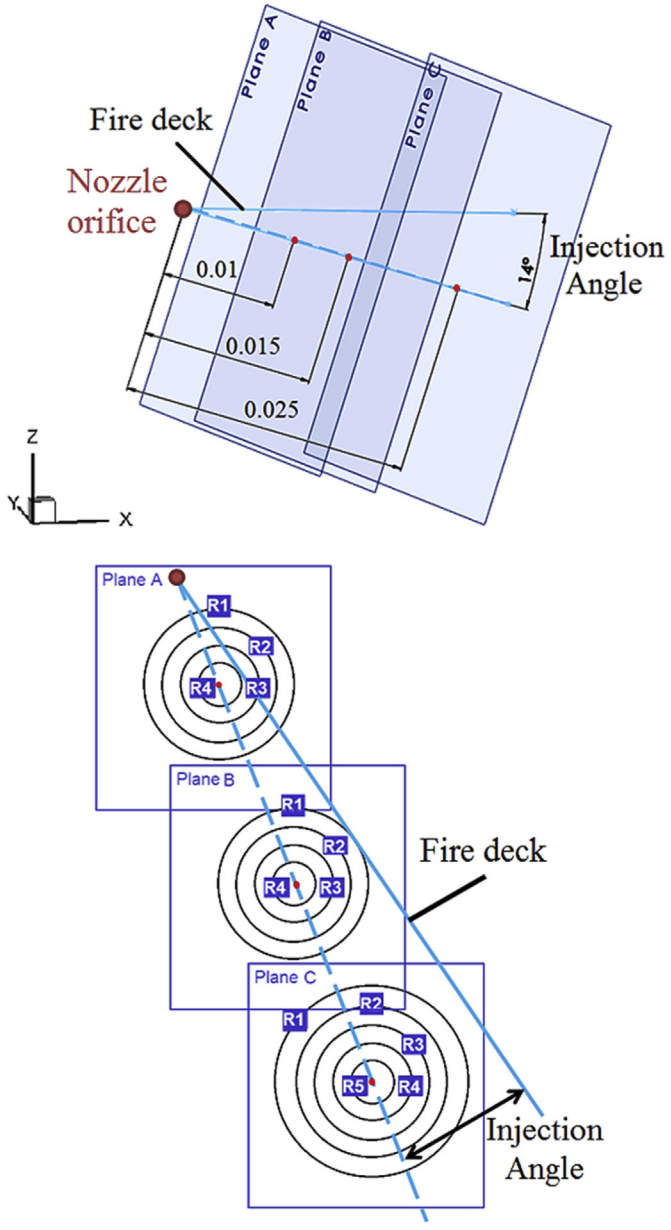

Fig. 8. Top: Planes A, B, and C parallel to the Plane III (Fig. 4) with the distances of 0.01, 0.015, and 0.025 [m] from the nozzle orifice, respectively. Bottom: Positions of R1−R4 in Planes A and B and R1−R5 in Plane C. Plane A: R1 = 2e−3, R2 = 1.5e−3, R3 = 1e−3, and R4 = 0.5e−3 [m]. Plane B: R1 = 3e−3, R2 = 2e−3, R3 = 1e−3, and R4 = 0.5e−3 [m]. Plane C: R1 = 5e−3, R2 = 4e−3, R3 = 3e−3, R4 = 2e−3, and R5 = 1e−3 [m].

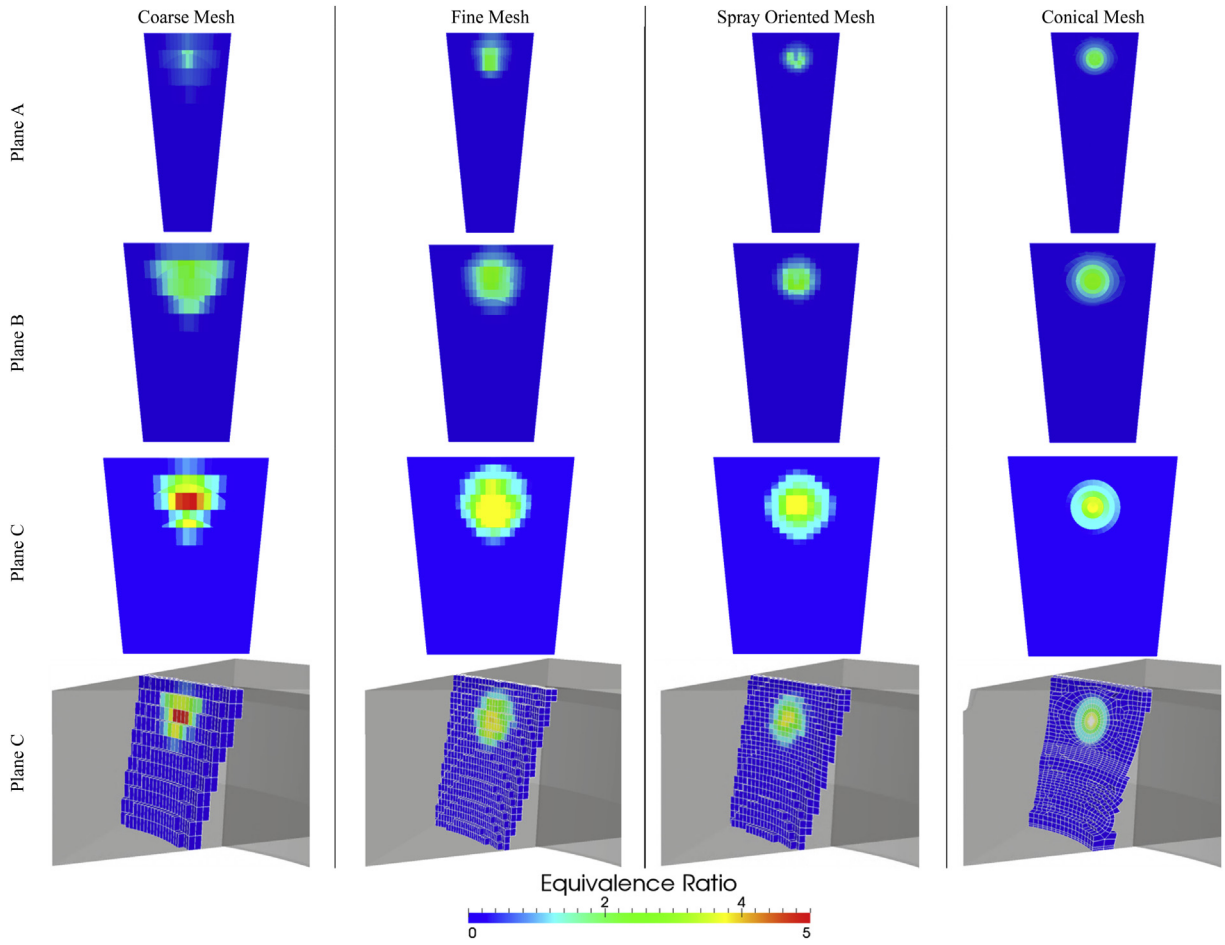

Fig. 9. Three top rows: Equivalence ratio distributions of four mesh types on a normal view of Planes A, B, and C at 3 CAD ATDC. Bottom: Computational cell alignments within the combustion chamber on the Plane C.

than 1 mm it had more density for higher U_x velocity. On the y coordinate, symmetrical distributions of U_y velocities were resulted for all grid types, whereas in z coordinates similar behavior discussed for x coordinates were resulted and Conical and Spray Oriented Mesh types represent lower numerical diffusion in vicinity of injector nozzle. In addition, more densities of higher velocities were resulted for Conical Mesh due to effective radial grid distribution showing the best agreement with the results of Gas-Jet theory.

3.2. Liquid and vapor penetration lengths

Singh et al. [7] conducted spray liquid and vapor penetration length measurements on SANDIA optical engine for different modes of combustion and have taken ten sample for penetration distances in each engine crank angle. A comparison of their experiments on the Low-Temperature Late-Injection case with the numerical predictions of four mesh types is shown in Fig. 4. Paying attention to the experimental results, it can be seen that there was a high level of cycle-to-cycle variations in the penetration length distances of ten samples in a particular crank angle. It should be noted that comparisons between numerical results in this study should be considered from SOI to start of ignition in the experiments as experiments were conducted under reacting conditions. Numerical simulations show acceptable trend in prediction of both liquid and vapor penetration lengths till start of ignition where the best agreement with the experiments for the applied DOI was achieved by the Conical Mesh. Fig. 4 also depicts noticeable difference on prediction of liquid and vapor penetrations between Corse and Fine Meshes, whereas the results for Spray Oriented and Conical Meshes were very close to each other. This can be discussed in a way that spray momentum was highly diffused to the vertices of the Coarse Mesh resulting in having the minimum penetration predictions. By refining the grid for the Fine Mesh, better results were obtained due to closer vertices to the Lagrangian parcels and lower spray momentum loss. Further enhancement of predictions in Spray Oriented and Conical Meshes, however, was not based on possessing higher cells but on their alignment. As it was mentioned in Section 2.2, Spray Oriented Mesh has lower cell count compared to the Fine mesh but its predictions show higher accuracy than the latter mesh type. This was mainly because Lagrangian parcels were spread in a higher number of cells in Fine Mesh causing higher momentum diffusion to the low momentum Eulerian cells during the Lagrangian–Eulerian coupling and finally reduction in the liquid and vapor penetration lengths. This would also affect the final delivered amount of evaporated fuel to an Eulerian cell, air–fuel mixing, and equivalence ratio distributions within the combustion chamber.

3.3. Liquid and gaseous fuel distribution contours

Fig. 5 compares the simulation results of liquid droplets (blue) and gaseous fuel (green) distributions using the four analyzed mesh types at 0, 2, 4, and 6 CAD ATDC with the experimental images. It should be noted that to capture experimental images, the

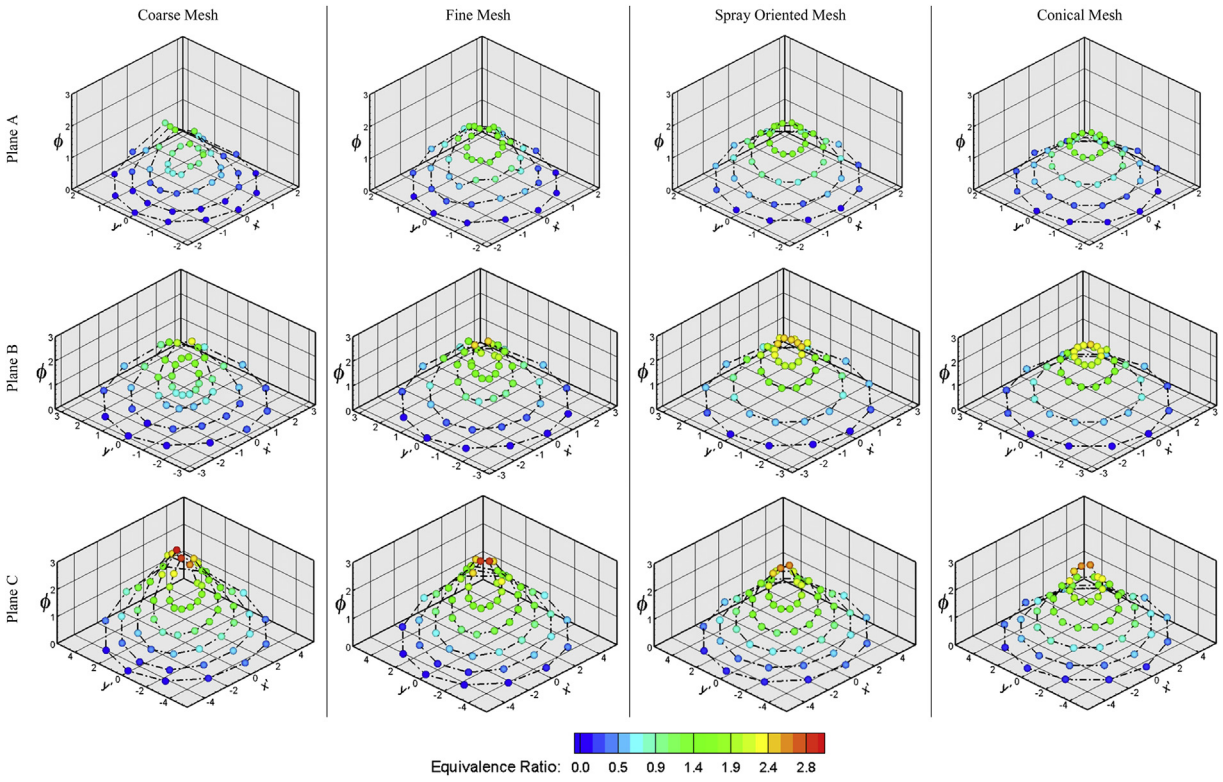

Fig. 10. Equivalence ratio magnitudes of R1−R4 on Planes A and B, and R1−R5 on Plane C at 3 CAD ATDC for four mesh types.

laser sheet was directed with the slope of 14° from the fire deck (injection angle) and later normal views of this plane were used to represent them. Similarly, normal views were selected to compare simulation results with the experiments of Singh et al. [7] for the Low-Temperature Late-Injection case in Fig. 5. As it can be seen, evolution of spray in the assigned DOI was well captured by both Spray Oriented and Conical Meshes where the latter mesh type shows the best agreement with the experiments. Results of liquid and gaseous fuel penetrations in Fig. 4 are shown tangible reduction when Coarse and Fine Meshes were applied. This coincides with the images of Fig. 5 where comparing to Conical and Spray Oriented Meshes, noticeably lower penetration lengths were resulted in Coarse and Fine Meshes. This behavior is because of higher drag forces on Lagrangian droplets as they face coarse Eulerian cells that were not oriented on the injection axis. Moving from the Coarse Mesh to the Conical Mesh in all the crank angles in Fig. 5, denser liquid core predictions were resulted. In Lagrangian droplet point of view, higher velocity loss was occurred in a fuel

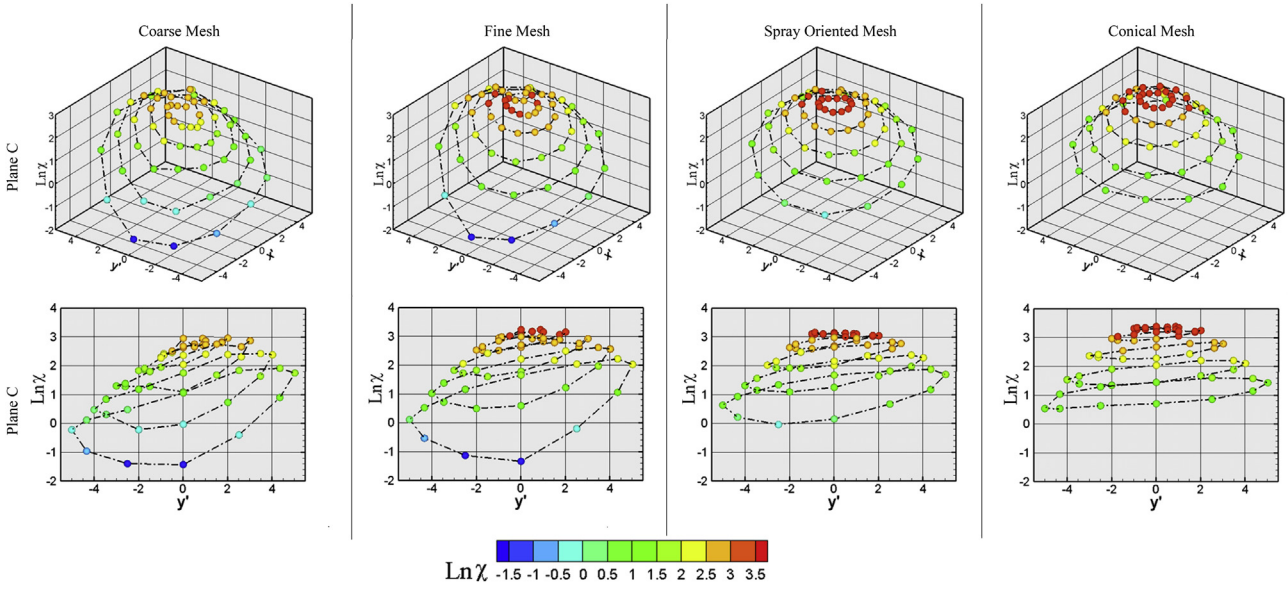

Fig. 11. 3D and 2D diagrams for scalar dissipation rate magnitudes of R1−R4 on Planes A and B, and R1−R5 on Plane C for four mesh types at 7 CAD ATDC.

droplet in the Coarse Mesh resulted in accelerated evaporation and diameter reduction due to its lengthy disposal to the hot Eulerian gas flow. In Eulerian gas point of view, only cells near to the nozzle orifice gain high momentum in the Coarse Mesh as due to coarser cell dimensions they were subjected to a large number of Lagrangian droplets. Accumulation of these two effects has resulted both in having sparser liquid core and shorter liquid and gas penetrations in coarse and non-spray oriented grids.

3.4. Equivalence ratio distribution

3.4.1. Plane I

Fig. 6 shows equivalence ratio distributions on Plane I for the applied mesh structures at 3 CAD ATDC as the mid of DOI. It can be seen that equivalence ratio distribution was highly affected by mesh types. Moving on the injection axis from the Coarse Mesh to the Conical Mesh, less equivalence ratio was resulted in the spray tip. For Plane I this behavior can be discussed together with the results of liquid and vapor fuel distributions in Fig. 5. Higher penetrations and lower spray momentum losses were resulted due to the enhanced mesh alignment and finer mesh structure in the Spray Oriented and Conical Meshes where such a trend was not reported in Coarse and Fine Meshes. At 3 CAD ATDC (mid of DOI) predicted particle velocities out of the injector orifice were the highest due to the injection profile [7]. Participation of these high momentum particles which newly introduced to the spray tail in mixing process is low as they need time to undergo the breakup, diameter reduction and evaporation processes. Taking high momentum particles in the spray tail and low momentum particles in the spray tip into consideration, as discussed it was expected equivalence ratio to increase from tail to tip. This trend was pronounced in Coarse and Fine Meshes due to higher momentum reduction in the spray tip and higher gradients of equivalence ratio were resulted comparing to Spray Oriented and Conical Meshes.

Advantage of Spray Oriented and Conical Meshes is represented in Fig. 6 for 3 CAD ATDC as mid time of injection duration. Results show that cross section on three dimensional equivalence ratio distributions using the Plane I was much closer to the actual conical spray structure comparing to the Coarse and Fine Meshes. It should be noted that mesh alignments in Coarse and Fine Meshes introduces poor and reticulated evaporated spray structure which is also shown in Fig. 6 by representing the computational cells making up equivalence ratio cross section on Plane I. This is a critical stage if later combustion simulations of the reacting flow would be conducted.

3.4.2. Plane II

Equivalence ratio distributions of the four mesh types are shown in Fig. 7 on the cross section of Plane II. Poor evaporated spray structure was resulted in Coarse and Fine Meshes, whereas proper mesh alignment in Spray Oriented and Conical Meshes was led to much lower departure from conical structure. Computational cells which occupy the volumes on Plane II cross section also show that applying Cartesian type of mesh alignment in Coarse and Fine Meshes would be resulted in more reticulated equivalence ratio distributions. It should be noted that by further refining the Fine Mesh it is possible to get closer to the conical structure but Spray Oriented Mesh was already fulfilled this with lower number of cells comparing to the Fine Mesh.

3.4.3. Plane III

Geometrical orientation of the Plane III is shown in Fig. 2. Keeping the normal vector of the Plane III constant, Fig. 8 (top) shows planes A, B, and C which were made by distances of 0.01, 0.015 and 0.025 [m] from the nozzle orifice on the injection axis, respectively. Results of equivalence ratio distributions for these planes using four mesh types are depicted in Fig. 9 at 3 CAD ATDC. Results show that only Conical Mesh alignment is capable of predicting accurate radial equivalence ratio distributions on the planes A, B, and C forming concentric circles around the injection axis. For instance, in all planes of the Coarse Mesh very poor distributions of equivalence ratio were resulted. Fine and Spray Oriented Meshes had better results comparing to the Coarse Mesh; however, equivalence ratio distribution was highly reticulated. This behavior was resulted from the mesh alignment which was also shown by the cells occupying the cross sections of the Plane C.

In order to discuss the magnitude of equivalence ratio distribution on Planes A, B, and C, four circles, R1−R4, were considered on Planes A, and B and five circles, R1−R5, on Plane C as shown in Fig. 8 (bottom). Simulated equivalence ratio data were sampled on twelve equally distanced points on the circles on the Planes A, B, and C and are shown in Fig. 10 for four mesh types at 3 CAD ATDC.

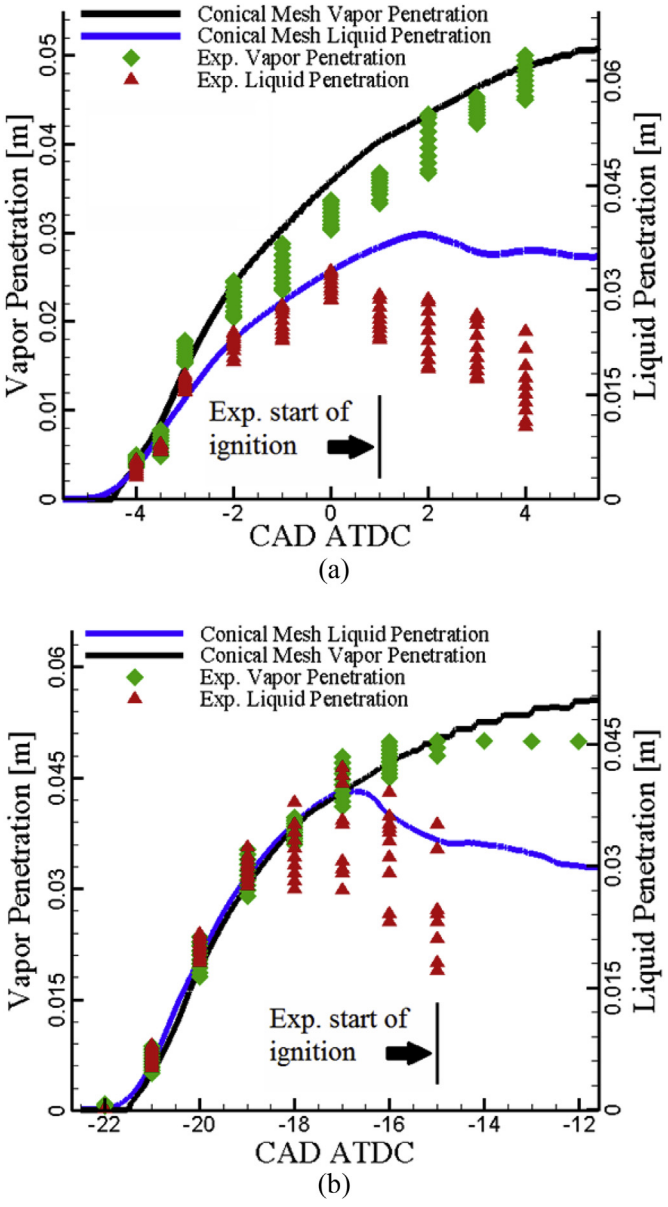

Fig. 12. Liquid and vapor penetration length comparisons between experiments of Singh et al. [7] and numerical simulations of (a) High-Temperature Long Ignition Delay and (b) Low-Temperature Early-Injection cases using the Conical Mesh.

Sampled data for these points was colored by magnitude of equivalence ratio and was shown using spheres at the points on the circles R1−R4 in Planes A, and B, and R1−R5 in Plane C. Using new $x'-y'$ coordinate systems diagrams in Fig. 10 show tangible fluctuations of equivalence ratio magnitude in Coarse and Fine Meshes when compared to their corresponding circles in the Spray Oriented and Conical Meshes. It should be noted that relations between points on circles were not linear this is why dashed lines were used to link the spheres together. Fig. 10 also shows that larger the momentum decay, higher the magnitude of equivalence ratio which coincides with the discussions on the previous sections.

3.5. Scalar dissipation rate distributions

Noticeable differences would be resulted in flame structure due to change in the values of $\tilde{\chi}$ as it is directly related to the preparation of combustible mixtures and chemistry−turbulence interactions. Fig. 11 represents the magnitudes of scalar dissipation rate for considered circles on Planes A, B, and C at 7 CAD ATDC (end of DOI). As this engine crank angle was the end of injection process, magnitudes of scalar dissipation rate would play a key role on heat release rate and emission formation if the reacting flow simulations would be conducted. It can be seen that lower values for $\tilde{\chi}$ were resulted at the end of injection for the Coarse Mesh, whereas a similar trend was not observed for three other mesh types. On the other hand, both 3D and 2D diagrams show less variation of scalar dissipation rate magnitudes by moving from the Coarse Mesh to the Conical Mesh. This would result in more uniform flame structure in Conical Mesh and it is acceptable due to low swirl combustion chamber of SANDIA optical engine.

4. Simulation of different operating conditions

In order to show the applicability of the Conical Mesh, simulations were conducted for two more engine operating conditions of High-Temperature Long Ignition Delay and Low-Temperature Early-Injection. Properties of these two cases are represented in Table 3. Non-reacting simulation results of liquid and vapor penetrations are shown in Fig. 12. It should be noted that experimental results were extracted under reacting conditions where heat release due to combustion was started at 1 and −17 CAD ATDC in High-Temperature Long Ignition Delay and Low-Temperature Early-Injection cases, respectively. From start of injection up to these engine crank angles results for liquid and vapor penetration lengths were showing an acceptable agreement in both cases using the Conical Mesh. Further validation of the Conical Mesh alignment for spatial liquid and vaporized fuel distributions can be seen in Fig. 13. Simulation results were compared with their corresponding experimental images at the engine crank angles as shown in Fig. 13 for High-Temperature Long Ignition Delay and Low-Temperature Early-Injection cases. It can be seen that predicted liquid and vaporized fuel distributions by the Conical Mesh was in a good agreement with the experimental images. However, simulations results were slightly over predicted comparing to the experiments which was acceptable as ignition and combustion simulations were not considered in the numerical modeling.

5. Conclusions

After discussing the conducted numerical simulations on enhancement of evaporated spray structure using the Conical Mesh

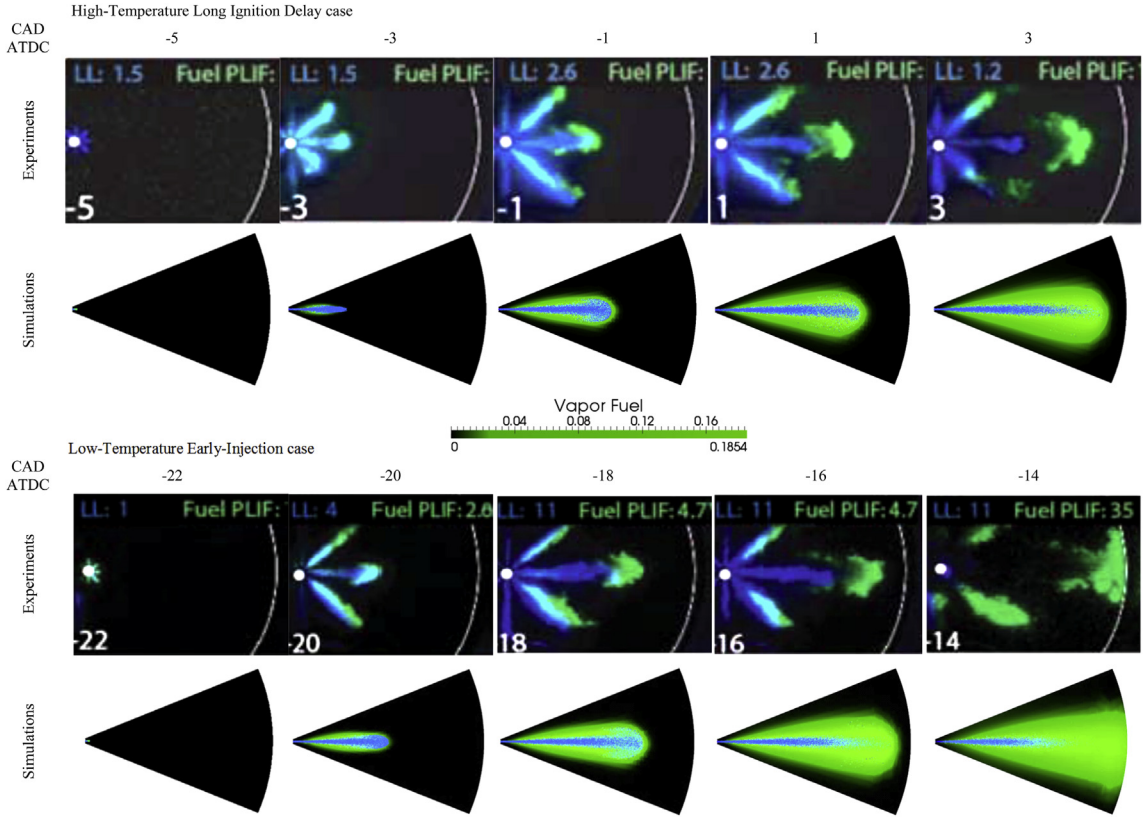

Fig. 13. Simulation results of liquid fuel particles (blue) and vaporized fuel mass fraction (green) distributions on the plane of spray injection axis for Conical Mesh at considered engine cranks of High-Temperature Long Ignition Delay and Low-Temperature Early-Injection cases compared to the experiments of Singh et al. [7]. (For interpretation of the references to color in this figure legend, the reader is referred to the web version of this article.)

and comparison of its results with Coarse, Fine, and Spray Oriented Meshes, the main conclusions were made below:

- By applying conical grid alignment lower numerical diffusion was resulted in vicinity of the injector nozzle where the churning flow takes place and spray morphology was enhanced downstream in evaporated spray region which showed less departure from the actual conical structure in the experiments.
- Higher magnitudes of equivalence ratio were resulted in early crank angles after initiation of injection process in Coarse and Fine Meshes. This was mainly due to high momentum diffusion and spread of Lagrangian particles to the large number of computational cells in Coarse and Fine Meshes, respectively. Similar trend was not observed for Spray Oriented Mesh with lower cell count comparing to the Fine Mesh.
- Application of coarser and non-spray oriented grid alignments resulted on both reticulated evaporated spray simulations and unacceptable early evaporation due to over estimations on momentum diffusion and lowered Lagrangian particle velocity and higher liquid fuel diameter reduction.
- Both Spray Oriented and Conical Meshes showed acceptable results for liquid and gaseous fuel penetration lengths. However, predictions for spray morphology on radial distances from the injection axis showed acceptable trend only for Conical Mesh alignment of the grids.

Acknowledgements

Authors would like to gratefully acknowledge contribution of Dr. Satbir Singh from Carnegie Mellon University for providing the experimental data and Dr. Mark PB Musculus from Sandia National Laboratories and Dr. Caroline Genzale from Georgia Institute of Technology for their assistance and useful discussions on the details of the engine experiments on maximizing accuracy of the presented numerical study.

References

[1] M.P.B. Musculus, P.C. Miles, L.M. Pickett, Conceptual models for partially premixed low-temperature diesel combustion (vol 39, pg 246, 2013), Prog. Energy Combust. 41 (2014) 94.
[2] M.K. Khair, W.A. Majewski , Diesel Emissions and Their Control, 2006. Vol. 303. SAE Technical Paper.
[3] C.L. Genzale, Rolf D. Reitz, Mark PB. Musculus, Effects of piston bowl geometry on mixture development and late-injection low-temperature combustion in a heavy-duty diesel engine, SAE Int. J. Engines 1 (1) (2009) 913–937.
[4] T. Kanda, Takazo Hakozaki, Tatsuya Uchimoto, Jyunichi Hatano, Naoto Kitayama, Hiroshi Sono, PCCI operation with early injection of conventional diesel fuel, SAE Trans. 114 (3) (2005) 584–593.
[5] C. Baumgarten, Mixture Formation in Internal Combustion Engines, Springer, Berlin, 2006.
[6] T. Lucchini, G. D'Errico, D. Ettorre, Numerical investigation of the spray–mesh–turbulence interactions for high-pressure, evaporating sprays at engine conditions, Int. J. Heat Fluid Flow 32 (2011) 285–297.
[7] S. Singh, R.D. Reitz, M.P.B. Musculus, T. Lachaux, Validation of engine combustion models against detailed in-cylinder optical diagnostics data for a heavy-duty compression-ignition engine, Int. J. Engine Res. 8 (2007) 97–126.
[8] S.J. Shuai, N. Abani, T. Yoshikawa, R.D. Reitz, S.W. Park, Evaluation of the effects of injection timing and rate-shape on diesel low temperature combustion using advanced CFD modeling, Fuel 88 (2009) 1235–1244.
[9] T. Lucchini, G. d'Errico, D. Ettorre, G. Ferrari, Numerical investigation of non-reacting and reacting diesel sprays in constant-volume vessels, SAE Int. J. Fuels Lubr. 2 (1) (2009) 966–975.
[10] P. Beard, Jean-Marc Duclos, Chawki Habchi, Gilles Bruneaux, Karim Mokaddem, T. Baritaud, Extension of Lagrangian–Eulerian Spray Modeling: Application to High Pressure Evaporating Diesel Sprays, 2000 (SAE Paper 2000-01-1893).
[11] J.J. Monaghan, Smoothed particle hydrodynamics, Annu. Rev. Astronom. Astrophys. 30 (1992) 543–574.
[12] G.Y. Zhang, X.Q. Qiao, X.L. Miao, J.H. Hong, J.B. Zheng, Effects of highly dispersed spray nozzle on fuel injection characteristics and emissions of heavy-duty diesel engine, Fuel 102 (2012) 666–673.
[13] C. Chartier, U. Aronsson, O. Andersson, R. Egnell, B. Johansson, Influence of jet–jet interactions on the lift-off length in an optical heavy-duty DI diesel engine, Fuel 112 (2013) 311–318.
[14] J. Li, W.M. Yang, H. An, A. Maghbouli, S.K. Chou, Effects of piston bowl geometry on combustion and emission characteristics of biodiesel fueled diesel engines, Fuel 120 (2014) 66–73.
[15] S.W. Park, Optimization of combustion chamber geometry for stoichiometric diesel combustion using a micro genetic algorithm, Fuel Process. Technol. 91 (2010) 1742–1752.
[16] S.L. Wei, F.H. Wang, X.Y. Leng, X. Liu, K.P. Ji, Numerical analysis on the effect of swirl ratios on swirl chamber combustion system of DI diesel engines, Energy Convers. Manag. 75 (2013) 184–190.
[17] D. Farrace, Michele Bolla, Yuri M. Wright, Konstantinos Boulouchos, Predicting in-cylinder soot in a heavy-duty diesel engine for variations in SOI and TDC temperature using the conditional moment closure model, SAE Int. J. Engines 6 (3) (2013) 1580–1593.
[18] Y. Imamori, Kenji Hiraoka, Shinsuke Murakami, Hiroyuki Endo, Christopher J. Rutland, Rolf D. Reitz, Effect of Mesh Structure in the KIVA-4 Code with a Less Mesh Dependent Spray Model for DI Diesel Engine Simulations, 2009 (SAE paper 2009-01-1937).
[19] Y. Li, Q. Xue, S. Kong, Z. Xu, J. Yi, D.J. Torres, Parallel Computing of Kiva-4 Using Adaptive Mesh Refinement, 2009 (SAE paper 2009-01-0723).
[20] Y.H. Li, S.C. Kong, Integration of parallel computation and dynamic mesh refinement for transient spray simulation, Comput. Meth. Appl. Mech. Eng. 198 (2009) 1596–1608.
[21] Q.L. Xue, S.C. Kong, Development of adaptive mesh refinement scheme for engine spray simulations, Comput. Fluids 38 (2009) 939–949.
[22] A.M. Lippert, Shengming Chang, Sasanka Are, David P. Schmidt, Mesh Independence and Adaptive Mech Refinement for Advanced Engine Spray Simulations, 2005 (SAE paper 2005-01-0207).
[23] M. Jia, M.Z. Xie, T.Y. Wang, Z.J. Peng, The effect of injection timing and intake valve close timing on performance and emissions of diesel PCCI engine with a full engine cycle CFD simulation, Appl. Energy 88 (2011) 2967–2975.
[24] M. Jia, Y.P. Li, M.Z. Xie, T.Y. Wang, Numerical evaluation of the potential of late intake valve closing strategy for diesel PCCI (premixed charge compression ignition) engine in a wide speed and load range, Energy 51 (2013) 203–215.
[25] R. Jhavar, Christopher J. Rutland, Effects of Mixing on Early Injection Diesel Combustion, 2005 (SAE paper 2005-01-0154).
[26] L. Cao, Amit Bhave, Haiyun Su, Sebastian Mosbach, Markus Kraft, Antonis Dris, Robert M. McDavid, Influence of Injection Timing and Piston Bowl Geometry on PCCI Combustion and Emissions, 2009 (SAE paper 2009-01-1102).
[27] Y. Yu, Wanhua Su, Haozhong Huang, Study of Fuel Distribution on Diesel PCCI Combustion by Development of a New Characteristic-time Combustion Model, 2008 (SAE paper 2008-01-1605).
[28] H.G. Weller, G. Tabor, H. Jasak, C. Fureby, A tensorial approach to computational continuum mechanics using object-oriented techniques, Comput. Phys. 12 (1998) 620–631.
[29] G.D.E.T. Lucchini, F. Brusiani, G.M. Bianchi, A finite-element based mesh motion technique for internal combustion engine simulations, in: The Seventh International Symposium on Diagnostics and Modeling of Combustion, Sapporo, 2008.
[30] G. Montenegro, A. Onorati, F. Piscaglia, G. D'Errico, Integrated 1D-MultiD Fluid Dynamic Models for the Simulation of I.C.E. Intake and Exhaust Systems, 2007 (SAE paper 2007-01-0495).
[31] P.A. Nordin, Complex Chemistry Modeling of Diesel Spray Combustion, Chalmers University of Technology, 2001.
[32] H. Pitsch, H. Barths, N. Peters, Three-dimensional Modeling of NOx and Soot Formation in DI-diesel Engines Using Detailed Chemistry Based on the Interactive Flamelet Approach, 1996 (SAE paper 962057).
[33] H. Barths, C. Hasse, N. Peters, Computational fluid dynamics modelling of non-premixed combustion in direct injection diesel engines, Int. J. Engine Res. 1 (3) (2000) 249–267.
[34] U. Egüz, Sridhar Ayyapureddi, Cemil Bekdemir, Bart Somers, Philip de Goey, Modeling Fuel Spray Auto-ignition Using the FGM Approach: Effect of Tabulation Method, 2012 (SAE paper 2012-01-0157).
[35] G. D'Errico, T. Lucchini, F. Contino, M. Jangi, X.-S. Bai, Comparison of well-mixed and multiple representative interactive flamelet approaches for diesel spray combustion modelling, Combust. Theory Model. (2013) 1–24.
[36] S. Singh, Rolf D. Reitz, Mark PB. Musculus, Comparison of the Characteristic Time (CTC), Representative Interactive Flamelet (RIF), and Direct Integration with Detailed Chemistry Combustion Models against Optical Diagnostic Data for Multi-mode Combustion in a Heavy-duty DI Diesel Engine, 2006 (SAE paper 2006-04-03).
[37] S. Singh, Rolf D. Reitz, Mark PB. Musculus, 2-Colorthermometry Experiments and High-speed Imaging of Multi-mode Diesel Engine Combustion, 2005 (SAE paper 2005-01-3842).
[38] K.Y. Huh, A.D. Gosman, A phenomenological model of diesel spray atomization, in: Proceedings of the International Conference on Multiphase Flows, 1991.
[39] R.D. Reitz, Modeling atomization processes in high-pressure vaporizing sprays, Atom. Spray Technol. 3 (1987) 309–337.
[40] G.M. Faeth, Mixing, transport and combustion in sprays, Prog. Energy Combust. 13 (1987) 293–345.
[41] N. Abani, A. Munnannur, R.D. Reitz, Reduction of numerical parameter dependencies in diesel spray models, J. Eng. Gas Turb. Power 130 (2008).